Probing the role of acid site distribution on water structure in aluminosilicate zeolites: insights from molecular dynamics

*Mingze Zheng and Brandon C. Bukowski**

Department of Chemical and Biomolecular Engineering, Johns Hopkins University, Baltimore, Maryland 21218, United States

ABSTRACT: Water plays a pivotal role in numerous chemical processes, especially in the production of fuels and fine chemicals derived from bio-based feedstocks. Zeolites are porous catalysts used extensively due to their shape-selective adsorption and confinement interactions; however the kinetics of zeolite-catalyzed reactions are significantly impacted by the presence of water, which may affect product selectivity and intrinsic rate constants depending on transition state polarity. In this study, we employed machine learning force fields (MLFFs) to accelerate *ab initio* molecular dynamics (AIMD) simulations and enhance the phase space exploration of water configurations in a mode Brønsted acid zeolite, H-AFI. We interrogated the structure of adsorbed water based on the Si/Al ratio and acid site distribution to disentangle the impact of acid site density and distribution on water matrix organization as a function of water loading. We integrated adsorption thermodynamics, vibrational spectroscopy simulations, and local density maps to interrogate the spatial orientation of adsorbed water clusters and their degree of hydrogen bonding. Our analysis unveiled the intricate interplay between zeolite structure, Brønsted acid site location, and water where spatially disparate acid sites nucleate extended clusters that span siliceous regions of the zeolite. We found that the length scale of ordered water regions is directly related to the Si/Al ratio and spatial distribution of Al sites. These findings provide insights into the molecular-level structure of water in microporous aluminosilicate micropores and demonstrate how acid sites can be used to control water activity which has applications to heterogeneous catalysis and adsorptive separations.

KEYWORDS: Zeolite, porous material, water, machine learning force fields, density functional theory, molecular dynamics

INTRODUCTION

Zeolites are nanoporous solids characterized by high crystallinity and hydrothermal stability that have been studied extensively due in part to their role as catalysts and sorbents for the petrochemical industry,[1–5] environmental remediation,[6–11], and sustainable chemical synthesis.[12–14] Notably, aluminosilicate zeolites possess anionic lattice charges resulting from aluminum heteroatom substitutions that are balanced by cations such as protons, which can function as catalytic active sites. The distinct coordination and confinement environments of aluminum atoms within the zeolite framework allow for cations and guest adsorbates to be accommodated in diverse void spaces, which are determined by the underlying pore architecture. The catalytic reactivity of a framework proton is determined by the stability of a proton on a bridging oxygen, which acts as a conjugate base (AlO_4^-).[15]

The distribution and location of intracrystalline aluminum sites within zeolite frameworks impact active site accessibility and product selectivity.[16] The strategic placement of aluminum enables targeted chemical transformations and shape-selectivity for the formation of desired products.[17,18] Understanding the relationship between acid site location and reactivity is pivotal for designing and optimizing zeolite catalysts. This understanding is facilitated by advanced characterization techniques and computational modeling, leading to highly efficient catalyst development for diverse catalytic processes such as methanol-to-olefins (MTO)[19,20] and Fischer–Tropsch synthesis.[21–23] Furthermore, acid site location also significantly affects the structure and energetics of guest molecules, including solvents, within the zeolite framework.

Water often has a prominent role in zeolites, especially in hydrophilic aluminosilicate zeolites, due to its large heat of adsorption and its frequent formation as a product in oxygenate chemistries.[12] Additionally, water acts as a solvent, which can directly affect the stability of confined transition states, especially those involving renewable feedstocks and polar reaction intermediates within the zeolite.[24–26] The protonation of water molecules can give rise to various structures, including Zundel and Eigen structures and the interplay between these structures further contributes to the rich behavior of water in zeolites.[27,28] However, the presence of water can also hinder reaction rates.[29] Water molecules tend to form clusters, limiting the accessibility of reactants to active sites and consequently reducing the reaction rate.[30] Moreover, coadsorbed water may participate in transition states, affecting intrinsic kinetics.[31] Despite its ubiquitous role, fundamental insights into water structuring in acid zeolites remain challenging due to the formation of hydrogen bonding networks and complex cluster geometries.[27,32–34] These characteristics also complicate experimental characterization techniques and contribute to the complexity of understanding water's behavior in zeolites.

Simulation methods play a critical role in this endeavor. Two commonly used approaches are classical parameterized force fields (FF) and Density Functional Theory (DFT), the latter explicitly includes electron interactions. While it is true that FF methods are primarily employed for tasks like diffusion or adsorption, reactive force fields have been developed for various classes of reactions.[35–37] These specialized force fields aim to bridge the gap between computational efficiency, as seen in traditional FF methods, and the ability to model bond-breaking and bond-formation processes, characteristic of catalytic reactions. On the other hand, DFT-based first-principles (FP) calculations provide an electron-level description of electronic structure and energetics, making them a crucial tool for studying

catalysis. However, it is important to acknowledge that DFT calculations are computationally more demanding.

Efficiently predicting interatomic potentials is crucial to understanding and modeling complex molecular systems. Traditional methods for fitting interatomic potentials, such as quantum chemical calculations including DFT are not only computationally intensive but demand substantial time and resources. Machine learning force fields (MLFFs) describe the potential energy as a function of atomic structure descriptors, and their parameters are optimized to reproduce training data obtained from FP calculations. MLFFs have been successfully applied to predict the properties of various systems, including phase transition[38–40], interfaces,[41] adsorption,[42] and reactions[43].

Machine learning potentials have also been developed to understand interactions between water and silica polymorphs including zeolites. Roy et al. developed reactive potentials for silicates using an equivariant neural network that captured water deprotonation and silica dimerization reactions.[44] Neural network potentials for aluminosilicate zeolites have been developed and applied by Erlebach et al. and Saha et al[45,46] which included interactions between water molecules and Brønsted acid sites using ten different zeolite structures. By understanding the molecular interactions between the solvent and zeolites, simulations can open new avenues for optimizing reaction kinetics to enable the development of more efficient and selective catalysts.

In this work, we examined adsorbed water behavior within AFI aluminosilicate zeolites based on their acid site distribution and Si/Al ratio (acid site density) as a model zeolite framework to determine the impact of these factors on water organization and hydrogen bonding interactions as a function of water loading in the framework. Our investigation focused on developing fundamental insights into how aluminum density and distribution affect water organization as a function of water loading in the framework. To enhance the sampling efficiency for the large configurational space of possible water structures, we adopted a strategy that leverages MLFFs to accelerate *ab initio* molecular dynamics (AIMD) simulations. The results unveil the role of specific aluminum next-nearest neighbor interactions on both the thermodynamics of water adsorption and the distribution of adsorbed water clusters. The findings underscore the relationship Brønsted acid site locations and protic solvents, which are relevant for liquid phase catalysis as well as oxygenate chemistries that co-produce water. These results have applications in designing catalysts with tunable control over adsorbed water matrices.

METHODOLOGY

Model Construction. A CIF for zeolite AFI was obtained from the International Zeolite Association (IZA) structure database.[47] One and two aluminum-substituted AFI zeolites (denoted here as H-AFI and 2H-AFI, labeled based on the number of aluminum heteroatoms and protons per unit cell) were built using the atomic simulation environment (ASE) which was also used to place adsorbate water molecules at their initial positions.[48] For 2H-AFI, we constructed four different configurations based on the different aluminum locations and denoted them as 2H-AFI-1, 2H-AFI-2, 2H-AFI-3, and 2H-AFI-4. AFI 1×1×2 supercells with Si/Al ratios of 11 and 23, which correspond to 4 and 2 aluminum per unit cell (denoted u.c.$^{-1}$), respectively, were constructed by replicating the optimized 2H-AFI-1 unit cell. The water loading was doubled to maintain consistent unit cell loading.

First Principles Calculations. All density functional theory (DFT) based AIMD simulations were performed by Vienna Ab initio Simulation Package 6.3 (VASP 6.3, abbreviated as VASP in the following discussion)[49–52] with exchange correlation function of Perdew-Burke-Ernzerhof (PBE)[53] in conjunction with D3 corrections,[54] and Becke-Johnson (BJ) was used as the damping function. While PBE+D3(BJ) is known to overestimate water binding energies, as noted in Stanciakova et al.,[55] we chose this functional because its ability to capture key interactions like the directional and spatial characteristics of hydrogen bonding and Van der Waals interactions at relatively high computational efficiency. These interactions are essential for capturing proton solvation and water vibrational frequencies and preserve the relative stabilities of different acid site configurations.

In this work, the planewave kinetic energy cutoff was set to 500 eV, while the tolerance for the self-consistent field (SCF) was set to 1×10^{-5} eV. Calculations were performed spin-polarized, and a single gamma k-point mesh was used. The time step was set to 0.5 fs. A Nosé-Hoover thermostat[56] was used to simulate the NVT ensemble at a temperature of 300 K.

Initial lattice constants for AFI were obtained from IZA and were optimized using VASP. Force criteria were set to 0.03 eV/Å with all other parameters the same as described above. The cell constants, a, b, and c were adjusted in VASP with the optimized values for a and b being 13.68 Å and c being 8.60 Å and were kept constant in subsequent simulations. The volume deviation of these optimized cell constants from the original a=b=13.83 Å and c=8.58 Å is 2.07%. Aluminum atoms replaced silicon atoms and protons were added to the oxygen atom next to each aluminum atom in the 12-membered ring to balance the charge, generate Brønsted acid sites, and expose the proton to adsorbates. We estimated the saturation loading of water using the accessible volume (199.88 Å^3) of zeolite AFI which accounts for 14.07% of the total volume (1420.60 Å^3), leading to an approximate equilibrium loading of 6 H_2O u.c.$^{-1}$. Once we determined the water loading, the 2H-AFI configurations with water molecules were optimized by VASP using the same simulation conditions to obtain the initial configurations for the following MD simulations. Example INCAR files and POSCAR-formatted structures are included in the Supporting Information.

On-the-fly Machine Learning Force Fields. Investigating the interactions of confined water with acid sites requires both long time-scale simulations and reactive interactions due to proton shuttling events. Simulations based on FP calculations, such as AIMD, explicitly calculate the forces acting on each ion based on their electronic structure. Conversely, simulation methods based on empirical parameters like force fields require solid fundamental knowledge of the given system to investigate the relevant interactions at an atomic level. The VASP on-the-fly MLFF[38,57,58] is a force field method that derives its parameters from first-principles calculations and employs a Bayesian active learning algorithm. The VASP on-the-fly MLFF includes radial and angular descriptors,[57] utilizing the Gaussian Approximation Potentials (GAP) method[59] and Smooth Overlap of Atomic positions (SOAP) descriptors.[60]

After obtaining the 0 K optimized aqueous 2H-AFI structures, we employed VASP on-the-fly MLFF simulations to 2H-AFI-1, 2H-AFI-2, and 2H-AFI-3 with all other simulation conditions the same as we used in the AIMD simulations. The total duration of each MLFF simulation was 215 ps, and the first 15 ps

were used for equilibration with the remaining 200 ps as production steps.

The accuracy of a trained MLFF is related to the frequency of FP calculations. More frequent FP calculations result in higher accuracy but significantly increase the computational demand. FP calculations were only carried out when the Bayesian error for the forces and spilling factors exceeded the threshold.[58,61] In this work, the MLFFs underwent refinement after each training step. Here, we define a 'training step' as an iteration in the machine learning process where the force field parameters are adjusted to better fit the training data. 'Refinement' refers to the process of further adjusting the force field parameters when the Bayesian error of the force exceeds the average maximum Bayesian error observed over the last 10 training steps, and the relative standard deviation is less than 0.2 in normalized units. This refinement process helps improve the accuracy of the MLFF by fine-tuning its predictions based on the latest available data.[58] We intended to set this refinement to obtain more DFT calculations while balancing the computational intensity. **Figure S1** shows the sequential progression of DFT step ratios over total DFT steps in the first 215 ps, where over 50% of the DFT steps were performed in the first 80 ps of the simulation in most cases. This indicates an improvement in the force field's predictive accuracy. Example force field files and INCARs for our training are included in the Supporting Information.

We assessed the accuracy of our MLFF simulations by both visually inspecting the obtained structures as well as quantifying the error in energies and forces. Example simulation trajectory is also provided in the SI. In each on-the-fly MLFF simulation, we thoroughly examined the geometry over the course of the simulation which included the AFI framework and water configurations. This ensured that our models did not exhibit unphysical bond formation or bond cleavage events. We calculated the as-training mean absolute error (MAE) for each aluminum distribution and water loading to quantify the energy and force error of our potential. The as-training MAE for energies across all models was 24 meV/atom and the as-training MAE for forces across all models averaged 0.81 eV/Å. These MAE values are comparibly higher than the literature reported values, especially those using neural network architectures, most likely caused in part by the proton solvation and transfer interactions which differ from previously reported systems[39–41,61] including metal slab,[42] and bimolecular interactions between water and methanediols[43]. To further evaluate whether the strategy pursued here captures the important interactions for this system, we calculated water stretching and bending modes along with electronic interactions of adsorbed water in zeolite AFI. Further comprehensive data is available in **Figure S2 a-c** and **Figure S3 a-c** for reference.

To test the structures obtained from the on-the-fly MLFF method, we performed 10 ps AIMD simulations of 2H-AFI-2 at 2 H_2O u.c.$^{-1}$ and 2H-AFI-1 at 5 H_2O u.c.$^{-1}$ to compare the distribution of adsorbed water molecules. These results are shown in **Figure S4**. The AIMD and the on-the fly MLFF method show similar time-averaged water adsorption structures, suggesting that the on-the-fly MLFF method predicts consistent adsorbed water configurations.

We conducted on-the-fly MLFF training simulations on three different aluminum distributions (2H-AFI-1, 2H-AFI-2, and 2H-AFI-3) while varying the water loading from 1-6 H_2O u.c.$^{-1}$ Our calculations indicated that the MLFF model of 2H-AFI-2 at a loading of 6 H_2O u.c.$^{-1}$ exhibited the lowest energy and force errors (with MAEs of 7.8 meV/atom and 0.79 eV/Å, respectively). We then used this trained potential for H-AFI and 2H-AFI-4.

We further performed a shorter 150 ps simulation using the same fitted potential on both 2H-AFI-1 and 2H-AFI-3, each at a water loading of 6 H_2O u.c.$^{-1}$, to compare whether models trained on different Al distributions had comparable adsorption energies. We calculated the average water adsorption energy and found that the adsorption energies differed by less than 0.08 eV H_2O^{-1} compared to the individually trained models.

Aluminum Incorporation Energy. The total aluminum incorporation energy was calculated by the following equation (1):

$$E_{inc,total} = (E_{xH-AFI} + \mathrm{x}E_{Si(OH)_4}) - \left(E_{Si-AFI} + \mathrm{x}E_{Al(OH)_3} + \mathrm{x}E_{H_2O,g}\right) \quad \text{(eq. 1)}$$

Here x denotes the number of substituted aluminums, E_{xH-AFI} and E_{Si-AFI} represent the potential energy of aluminum incorporated AFI and siliceous AFI, respectively. $E_{Si(OH)_4}$, $E_{Al(OH)_3}$, and E_{H_2O} denote the potential energy of $Si(OH)_4$, $Al(OH)_3$, and H_2O in the gas phase. The configurations of AFI, H-AFI, and 2H-AFI were obtained from geometry optimizations.

Adsorption Thermodynamics. To make meaningful comparisons for adsorption energies, it is essential to establish uniform reference states. We performed an additional 10 ps MD simulations from the equilibrated structures using our trained potential (2H-AFI-2 at 6 H_2O u.c.$^{-1}$) for all water loadings and calculated the water adsorption energy per water molecule at 300 K by equation (2).

$$\overline{\langle E_{ads,p}\rangle} = \frac{\langle E_{nW+Z,p}\rangle - \langle E_{Z,p}\rangle - n_{water}\,\overline{\langle E_{W,p}\rangle}}{n_{water}} \quad \text{(eq. 2)}$$

Here, $\langle E_{nW+Z,p}\rangle$ and $\langle E_{Z,p}\rangle$ are the average total energy of the zeolite with n adsorbed water and the average potential energy of the framework obtained from 10 ps MLFF simulations using the trained force field, respectively. A liquid phase reference state was calculated from bulk water comprising 45 water molecules obtained from a 10 ps prediction simulation utilizing the same model as above to ensure a consistent thermodynamic reference state and represented as $\overline{\langle E_{W,p}\rangle}$. We then normalized the potential energy per water molecule using equation (3). This normalization accounts for various interactions between water molecules, including Coulomb and van der Waals interactions.[62]

$$\overline{\langle E_{W,p}\rangle} = \frac{\langle E_{W,bulk,p}\rangle}{45} \quad \text{(eq.3)}$$

Radial Distribution Functions. Aluminum-water radial distribution functions (RDFs) were computed by obtaining the interatomic distances between the aluminum and the oxygen atoms belonging to water molecules. All RDFs were normalized by the total peak area.

Water Density Plots. We generated time-averaged heatmaps that illustrate water density distribution by slicing perpendicular to the AFI center pore which corresponds to the [001] plane. Higher brightness in the heatmaps indicates a higher probability of water molecules visiting that region. Each heatmap encompasses the whole 215 ps simulation data. To improve clarity, we centered the AFI pore, making it easier to visualize the water distribution. In these heatmaps, water positions are represented by the oxygen atoms within the water molecules.

RESULTS AND DISCUSSION

Zeolite AFI structure. AFI is a one-dimensional framework structure characterized by identical T-sites. **Figure 1** depicts a 2 by 2 by 1 supercell to illustrate aluminum atom positions, although all simulations were conducted using a single unit cell. A potential aluminum atom location in H-AFI is colored blue and labeled by a star. A second aluminum atom was placed relative to the position of the first aluminum. Aluminum distribution in zeolites must obey Löwenstein's rule to avoid Al-O-Al bonds, which could lead to highly unstable structures.[63] We first explored three aluminum locations (represented by green atoms and labeled 1 to 3) for the second aluminum atom, which are next-nearest neighbors to the first aluminum substitution. These configurations were selected to represent unique combinations of aluminum positions relative to the anchoring initial aluminum. We note that the AFI unit cell can be divided into two SiO_2 layers along the z-axis. Specifically, the first and the third positions of the second aluminum atom align with the same layer as the anchor aluminum, while the second position, although having a similar Al-Al closest geometric distance as the third position, sits in a different layer.

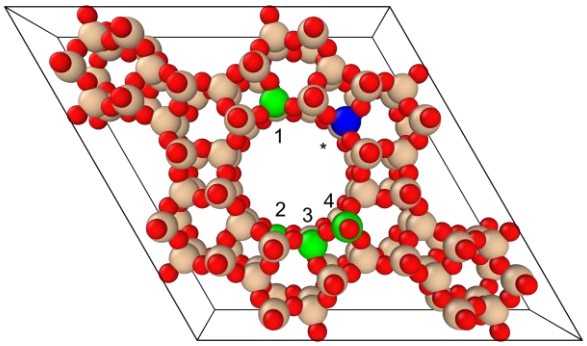

Figure 1. A 2x2x1 supercell of zeolite AFI with O colored red, and Si colored tan. Plausible locations for the next-nearest neighbor aluminum (marked as 1, 2, and 3) and the third nearest neighbor aluminum (marked as 4) substitutions are labeled in green relative to the initial aluminum substitution labeled in blue.

To increase the range of Al-Al distances while maintaining Löwenstein's rule, we explored a fourth aluminum position. Here the second aluminum location was chosen to be the third nearest neighbor to the anchoring aluminum (blue star) and situated in the same layer as the first and third positions. **Table 1** presents the distances between two aluminum atoms as both the minimum geometric distance, and distance across the AFI center pore. For all further analysis, we used the Al-Al distance across the pore as that measures the interaction length for water molecules within a single pore.

The single T-site in AFI makes it a model material to interrogate site distribution effects by removing the local structure differences around each Al site. We calculated Al incorporation energies and found that they differ by at most 0.14 eV (**Table 1**) indicating that the thermodynamics of heteroatom substitution do not significantly depend on which Si atom we choose.

Adsorbed water structure. We observed a variety of adsorbed water structures within AFI which are not only indicative of the dynamic nature of water molecule interactions, but also highlight hydrogen bonding at different acid site proximities.

At low water loading of 2 H_2O u.c.$^{-1}$ in 2H-AFI, direct water adsorption to the Al acid sites was evident (see **Figure 2a-b)**. A notable observation is that 2H-AFI structures with larger Al-Al distances (**Figure 2b**) exhibits a H_3O^+ planar triangular structure at each Al site, while 2H-AFI structures with closer distances (**Figure 2a**) exhibits a Zundel-like structure formed by two water molecules. In both cases, we found that the H_3O^+ ion is mainly interacting with Al adjacent O atom but remains bound to the acid site.

Table 1. Aluminum-aluminum distances and their incorporation energy calculated for each acid site distribution considered.

Al distribution	Al-Al shortest distance (Å)	Al-Al distance across the pore (Å)	Incorporation energy (eV)
2H-AFI-1	5.55	5.55	-2.38
2H-AFI-2	5.00	11.50	-2.51
2H-AFI-3	4.98	9.63	-2.49
2H-AFI-4	8.01	8.20	-2.37

Our simulations revealed the frequent occurrence of Zundel structures, especially at higher water loadings (3 - 6 H_2O u.c^{-1}), as illustrated in **Figure 2c-d**. This finding aligns with previous results from Hack et al.[64] For Zundel structures, a hydronium cation (H_3O^+) closely associated with a neighboring water molecule, forms a symmetric $H_5O_2^+$ complex, pivotal in the Grotthuss mechanism.[65] For the 4 H_2O u.c.$^{-1}$ water loading, both Zundel and Eigen structure was observed in 2H-AFI-2 (**Figure 2f**). The cis-Zundel isomer of $H_9O_4^+$ was identified within the adsorbed water in 2H-AFI-2 pore, while the Eigen isomer of $H_9O_4^+$ was found with one framework oxygen as proton receiver. On the contrary, no stable $H_9O_4^+$ Zundel isomer was observed in 2H-AFI-1 due to the close Al-Al distance (**Figure 2e**). These observations align with our thermodynamic analysis in **Figure 3**, where we find overall weaker water adsorption in 2H-AFI-1 compared to other 2H-AFI frameworks at this range of water loading.

Approaching the saturation water loading of 5 – 6 H_2O u.c.$^{-1}$, similar Zundel and Eigen structures can be observed (**Figure 2 g-h**), extending in the x-y plane and along the z-axis. In this case, we hypothesize that the strong Coulomb interactions in 2H-AFI with smaller Al-Al distances lead to the formation of denser water clusters (**Figure 2g**) which decreases the per-water adsorption energies shown in **Figure 3**. This clustering behavior is further supported in the radial distribution functions in **Figure 5** which are discussed below.

The presence of Zundel and Eigen complexes within the zeolite AFI pores underscore the prevalence of dynamic proton transfer events. These complexes, characterized by their rapidly fluctuating hydrogen bond networks, facilitate the proton shuttling process.

Water adsorption at different acid site distributions. We explored the relationship between water adsorption energy, water loading, and acid site distribution, with a focus on how acid site distribution influences water molecule reorganization. We first interrogated the role of water loading by calculating the time-averaged adsorption energies. **Figure 3** shows the variation of the water adsorption energy per water molecule as a function of the water loading. Our results indicate that the average water adsorption energy becomes less favorable as the water loading increases from 2 to 6 H_2O u.c.$^{-1}$ in both H-AFI and 2H-AFI.

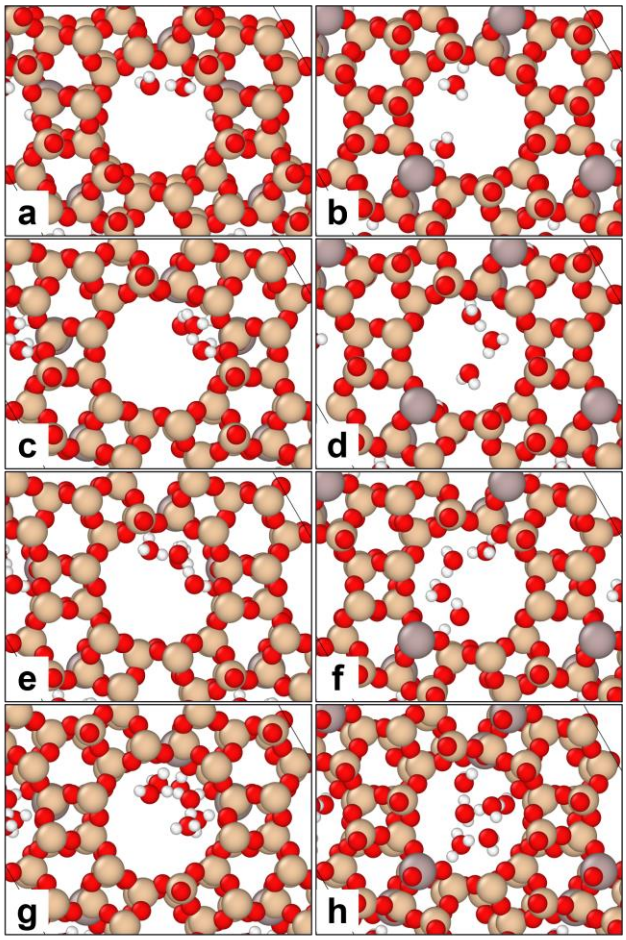

Figure 2. Representative snapshots of adsorbed water structures at water loading of 2, 3, 4, 6 H_2O u.c.$^{-1}$ in 2H-AFI-1 (**a**, **c**, **e**, and **g**) and 2H-AFI-2 (**b**, **d**, **f**, and **h**) obtained over the course of MD simulations.

This observation aligns with previous studies, such as those by Mei and Lercher on zeolite Beta,[28].

In AFI zeolites with 2 Al u.c.$^{-1}$, we observed varying adsorption behavior at different water loadings. Specifically, at the lowest loading of 1 H_2O u.c.$^{-1}$, the Al distribution becomes irrelevant as only one acid site is occupied by a water molecule. At water loadings between 2 – 6 H_2O u.c.$^{-1}$, water adsorption is less favorable in 2H-AFI-1, which had the shortest aluminum-to-aluminum distance across the pore.

In 1 Al u.c.$^{-1}$ AFI, water adsorption energy at loadings of 2 to 3 H_2O u.c.$^{-1}$ was generally less favorable compared to that in 2H-AFI. This is primarily due to the absence of a second proton that could stabilize the adsorbed water structure. As we approach the saturation loading (4 - 6 H_2O u.c.$^{-1}$), the adsorption behavior starts to resemble that observed in 2H-AFI, with hydrogen bonding dominating the energetics.

Our observations reveal a correlation between the water adsorption energy and water loading, with acid site distribution playing a role in modulating this relationship. We have seen that, as water loading increases, the average water adsorption energy becomes less favorable, a trend consistent across different zeolite systems. This decrease in adsorption energy can be attributed to the interplay between two primary factors: direct adsorption of water at the acid site and the formation of hydrogen bonds. In our earlier analysis, we discussed how, at lower water loadings (1 - 3 H_2O u.c.$^{-1}$), adsorption is primarily influenced by electrostatic interactions with the framework proton, resulting in higher adsorption energy. As we moved to higher water loadings (4 - 6 H_2O u.c.$^{-1}$), we observed a transition where hydrogen bond network formation among water molecules becomes significant. This network stabilizes different adsorbate configurations, diminishing the role of direct adsorption when normalized per water molecule. At even higher water loadings, the dominant factor in adsorption energy shifts from direct interactions of water molecules with the acid site to intermolecular interactions, such as the formation of hydrogen bonds, proton transfer, and interatomic interactions.[28] This shift in adsorbed water behavior aligns with our earlier discussion of adsorbed water structures. Together, these observations support our hypothesis that water adsorption energy is influenced by a combination of direct adsorption and hydrogen bond formation, with the specific mechanism depending on the water loading and acid site distribution.

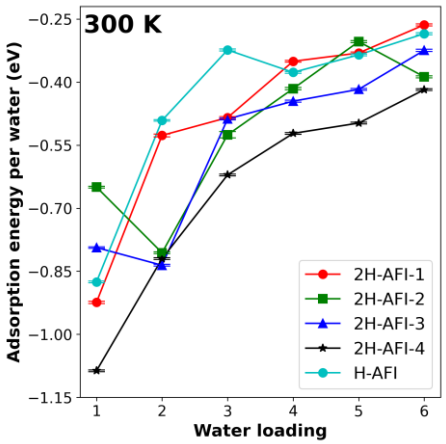

Figure 3. Water adsorption energy per water molecule with the increasing Al-Al distance across the AFI center pore. Error bars indicate the standard deviation for each system.

Adsorbed water clustering. To complement our study of adsorbed water MD snapshots and thermodynamic analysis, we tracked the position of water molecules over time in our simulations and studied the time averaged positions of adsorbed water clusters. The behavior of water molecules within the AFI center pore was studied as a function of water loading. **Figure 4** shows a subset of heatmaps that illustrate the local density of water within the AFI center pore, with the complete set of water density heatmaps included in **Figure S5 a-e**. Brighter regions of the density map indicate where water molecules are more frequently located, suggesting the presence of favorable adsorbed water structures within those regions.

For water loadings below 3 H_2O u.c.$^{-1}$, we find that water molecules cluster around the acid sites throughout the duration of the simulation. As the water loading increases, the water distribution extends throughout the central pore. At the saturation loading, we observe that water molecules access the full volume of the AFI center pore space regardless of the aluminum location and distribution.

To illustrate the effect of varying water loading, we chose a representative aluminum distribution (2H-AFI-2) and plotted the density heat maps from 1-6 H_2O u.c.$^{-1}$ (**Figure 4a-d**). We see that the water molecule was adsorbed at a single site, showing a single bright region localized near the Al heteroatom indicated

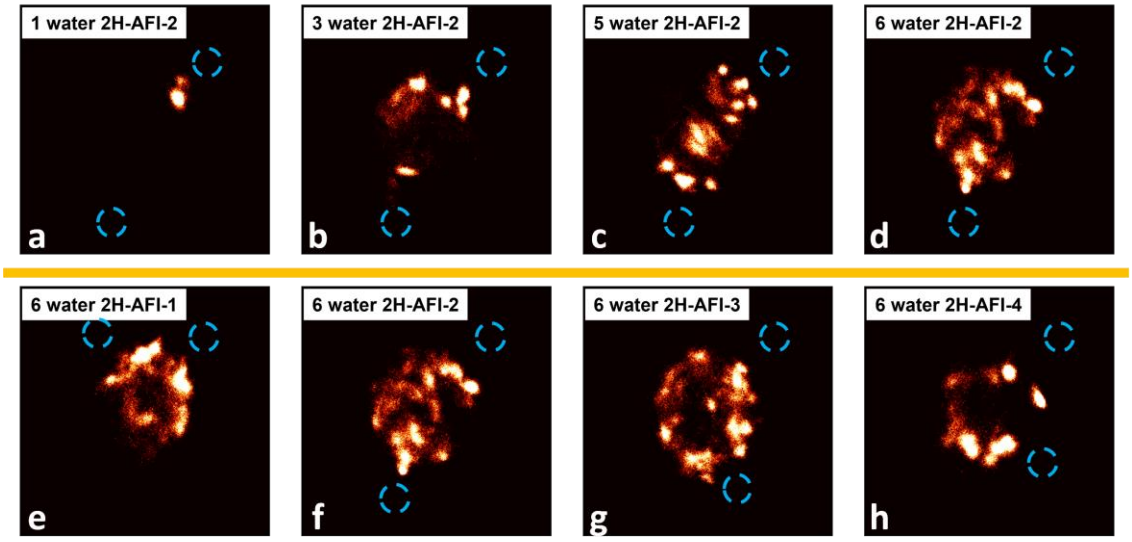

Figure 4. Time-averaged heatmaps of the water density distribution in AFI center pore viewed along the [001] plane. The zeolite framework is not shown. (a) to (d) are 2H-AFI-2 with one, three, five and six H_2O u.c.$^{-1}$ and (e) to (h) are 2H-AFI-1 to 2H-AFI-4 at the saturation water loading. Blue circles indicate the position of Al substituted heteroatoms. A complete set of density maps at all water loadings and aluminum distributions are included in **Supplementary Figure S5 a-e**.

by the blue circle. At 3 H_2O u.c.$^{-1}$ water molecules populate both Al sites as well as the central pore. At 5 H_2O u.c.$^{-1}$, an extended water cluster that spans both Al sites emerges which then saturates the accessible pore volume at 6 H_2O u.c.$^{-1}$.

At the saturation loading, we observed differences in the adsorbed water structure depending on the Al distribution. We found that larger Al-Al distances promoted the formation of broader water clusters, contributing to the stabilization of the water network within the zeolite AFI center pore (**Figure 4e-h**). For the shortest Al-Al distance (2H-AFI-1), the local density of water is more concentrated proximal to the two Al sites with minimal exploration of the siliceous region along the outer pore wall. This differs from the other distributions where distinct water clustering is observed which encompasses the full pore volume. The observed differences in equilibrium water density in conjunction with adsorption thermodynamics indicate that Al distribution can modulate both the thermodynamic stability and structure of adsorbed water.

Radial distribution functions of adsorbed water. We calculated radial distribution functions (RDFs) of oxygen atoms in the water molecules with respect to aluminum heteroatoms as a function of adsorbed water loading. Detailed RDFs for each water loading and Al distribution are provided in **Figure S6 a-e**. We will focus our comparisons on the shortest Al-Al distance (2H-AFI-1) and the largest Al-Al distance (2H-AFI-2).

At a loading of 2 H_2O u.c.$^{-1}$ (**Figure 5a**), distinct RDF behaviors were noted between 2H-AFI-1 and 2H-AFI-2. In 2H-AFI-1, the RDF presents a broad and split first peak, indicating the formation of water-water Zundel structure near the Al sites as shown in **Figure 2a**. Conversely, the RDF in 2H-AFI-2 displays a sharp first peak, suggesting a more uniform water-zeolite Zundel structure and closer proximity of water molecules to Al sites. The subsequent peaks, particularly between 5 – 7 Å, reflect interactions of water molecules with non-adjacent Al heteroatoms. This variation aligns with our findings from **Figure 2b**, where in sparser 2H-AFI configurations, each Al site is populated by one water molecule, leading to similar water adsorption.

When the water loading increases to 3 H_2O u.c.$^{-1}$, the broader peak profile in 2H-AFI-2 indicates more structured adsorbed water configuration across the pore. This broader peak correlates with the formation of the Zundel structure, as illustrated in **Figure 2d**. On the contrary, the narrower peak profile in 2H-AFI-1 indicates a more compact water configuration near the Al sites, reflecting a denser clustering of water molecules.

As water loading increases to 4 H_2O u.c.$^{-1}$, the first peaks from the RDFs of both 2H-AFI-1 and 2H-AFI-2 exhibit similar

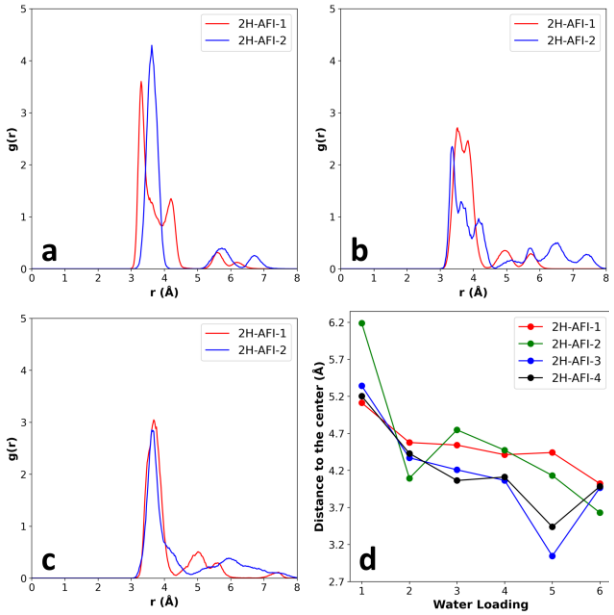

Figure 5. Radial distribution functions for water oxygen atoms and Al heteroatoms with the water loading of 2, 3, and 4 H_2O u.c.$^{-1}$ (**a**, **b**, **c**). Blue and red lines are the water RDFs in the Al distribution with smallest and largest Al-Al distance, respectively. (**d**) Average distances between protons and the AFI pore center.

shapes and center positions. This similarity suggests a convergence in the spatial distribution of water molecules closest to the Al sites for both configurations. However, a difference is observed in the subsequent peaks. In 2H-AFI-1, the subsequent peaks are sharper than 2H-AFI-2 indicating higher ordering in 2H-AFI-1 at longer distances while 2H-AFI-2 demonstrates more disordered bulk-like water. The RDF analysis provides a quantitative comparison between different Al-Al differences that reinforce our observations from the density heat maps and correlates with the adsorption energy trends.

Proton solubility. In addition to tracking the position of water molecules, we tracked the position of protons to determine their solubility in the pore centers. Previous studies from Mei, Rousseau, Lercher, and coworkers have shown that proton solubility depends on the number of coadsorbed waters.[66,67] Since we cannot *a priori* label protons in our system due to proton shuttling events, we calculated proton identities dynamically over the simulation. To do this, we generated neighbor lists for each oxygen and hydrogen atom excluding framework oxygens at each simulation step. The proton identity was then determined at each frame of the simulation by pairing hydrogens with oxygens based on the neighbor lists, and then determining which hydrogens had the largest H-O distance. These hydrogens were then labeled as a proton in that frame.

We sought to determine whether Al distributions affected the proton solubilities. **Figure 5d** illustrates the average distances of the framework protons to the AFI pore center in all four 2H-AFI configurations (i.e. a distance to the center of 0 Å would be the center of the pore). At 1 H_2O u.c.$^{-1}$, we note large distance values indicating protons remain close to the framework. As the water loading increases, the average distance in all configurations decreases, indicating protonation of adsorbed water and solvation into the cluster. This observation aligns with previous literature at high Si/Al ratios,[30] and in faujasite[46] which reported similar trends of proton solvation assisted by coadsorbed water. We noticed that all Al distributions exhibit a similar trend in proton distance with near-saturation loadings having average proton locations closest to the pore center. These data would indicate that protons solvate near the center of the pore more frequently on average when there are sufficient water molecules adsorbed. We did not find solubility to depend appreciably on the relative position of the acid sites under these conditions, but this opens questions into whether different pore topologies or temperatures could be used to control proton location.

Vibrational spectra of adsorbed water. We interrogated the hydrogen bond strength as a function of water loading by comparing water bending and stretching modes. These modes were compared by calculating the vibrational density of state (vDOS) which is shown in **Figure 6**. vDOS spectra were obtained using an in-house python module based on the atomic velocities using established techniques.[32] The dashed lines denote literature values for the vibrational frequencies of both liquid water and water vapor.[34] We observed shifts in the bending and stretching modes as water loading increased and as we changed aluminum distribution. As the water loading increased, both the frequencies associated with bending and stretching modes exhibited broader peak profiles, while remaining within a reasonable range that would be expected for water. The observed range of bending and stretching vibrational frequencies further indicates that our MLFF strategy captures the intermolecular forces present in water. At the saturation loading, we observed a shift in the stretching peak from 3746 cm^{-1} to 3448 cm^{-1} as the Al-Al distance increased. A decrease in the stretching peak has been shown to describe stronger hydrogen bonding.[68] These data indicate that disparate Al sites that nucleate extended water clusters form stronger hydrogen bonding networks than proximal Al sites.

Variation in Si/Al ratio. We then changed the Si/Al ratio to interrogate how Al density affects water cluster nucleation. We chose a single Al distribution (2H-AFI-2) and then expanded the simulation box by doubling its size along the AFI center pore. **Figure 7a-b** illustrates the water density distribution heat map along the zeolite AFI center cage which corresponds to the [010] plane. Here, **Figure 7a** illustrates the saturation loading of water at Si/Al 11 and subplot b illustrates the saturation loading of water at Si/Al 23. A Si/Al 11 corresponds to four aluminum atoms per supercell and Si/Al 23 corresponds to two aluminum atoms per supercell. We observed that Si/Al 23 exhibits a higher degree of clustering around the aluminum sites than the Si/Al 11 configuration which has water molecules adsorbed near both sets of Al sites marked in blue circles. To quantify the water structure around these acid sites, we calculated RDFs which are shown in **Figure 7c**. Both Si/Al 11 and Si/Al 23 RDFs exhibited a similar position for the first peak, indicating a consistent average distance between the first coordination shell of water molecules around acid sites. Si/Al 11 has a sharper RDF beyond the first peak as compared to Si/Al 23 which suggests that Si/Al 11 produces a more structured water environment than Si/Al 23. Si/Al 23 exhibited broader RDF peaks which indicate that intraporous water is more evenly distributed along the center pore in comparison. At higher Si/Al ratio we observed clustering around acid sites, but more disordered liquid-like water fills the siliceous intraporous region.

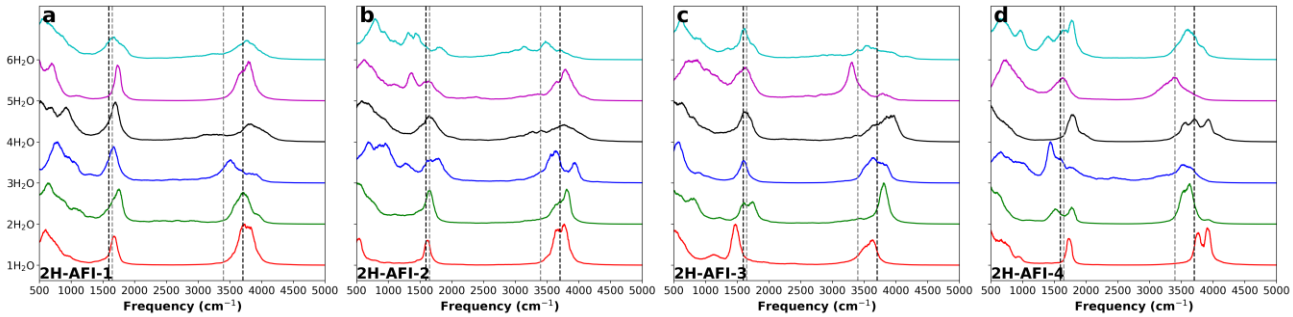

Figure 6. Vibrational density of state (vDOS) of water with different water loading in (**a**) 2H-AFI-1, (**b**) 2H-AFI-2, (**c**) 2H-AFI-3, and (**d**) 2H-AFI-4. Black dashed lines are reference gas water bending and stretching frequency, and grey dashed lines are reference liquid water bending and stretching frequency.[34]

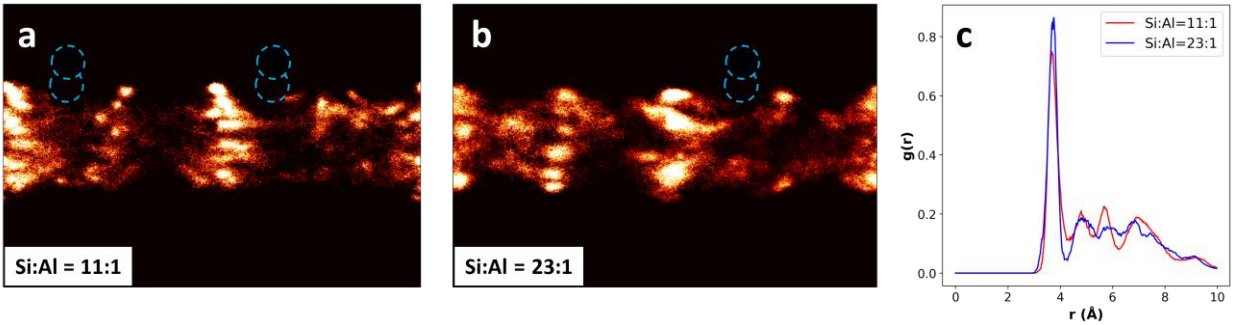

Figure 7. Heatmaps of the water density distribution along the AFI center pore in supercells with (**a**) Si/Al 11, (**b**) Si/Al 23, and (**c**) water RDFs for both Si/Al ratios.

The lower Si/Al ratio leads to extended water clusters where a greater degree of water structuring was observed indicating that acid site proximity plays a role in the spatial extent of water clustering.

CONCLUSION

Our investigation into water structuring provides insights into the intricate relationship between aluminum density and distribution within AFI aluminosilicate zeolites and the organization of adsorbed water molecules as a function of water loading. Using on-the-fly MLFFs to expedite AIMD simulations and improve the sampling of diverse water configurations, we have obtained a deeper understanding of the role played by specific aluminum distributions in the thermodynamics of water adsorption and the spatial arrangement and persistence of water clusters in zeolite AFI. Notably, we observed a consistent decrease in water adsorption energies with increasing water loading, which is influenced by both the distribution and density of Al in the AFI structure. Additionally, at higher water loadings, we discovered a tendency for water clusters to form, especially around framework protons, which play a crucial role in stabilizing these clusters. These findings were corroborated by independent computational characterization methods including density maps, radial distribution functions, proton locations, and vibrational spectra. The union of these data indicates that spatially disparate Al sites better stabilize extended hydrogen bonding networks. At high Si/Al ratios, water clusters nucleate in isolation, with intraporous disordered water filling the siliceous regions. As the Si/Al ratio decreases, water clusters interact which leads to larger clusters with strong hydrogen bonding.

These findings underscore the interplay between confined structure, Brønsted acid site location, and water adsorption, providing evidence that precise control over Si/Al ratio and distribution will directly influence the structure and stability of adsorbed water matrices. This may play a role in liquid-phase catalysis and oxygenate chemistries involving water co-generation where adsorption, diffusion, and transition state stability are affected by the water activity. This approach has implications for future studies that link the cluster geometries observed here with the kinetics of reactions catalyzed by zeolites or other porous materials. These findings provide evidence that controlling the microenvironments around catalytic active sites can tailor water activity.

ASSOCIATED CONTENT

Supporting Information

Procedures and simulation details (PDF). ZIP folder containing simulation settings, structures for bulk water, H-AFI, 2H-AFI, supercells, and MLFF model for 2H-AFI-2.

AUTHOR INFORMATION

Corresponding Author

* Brandon C. Bukowski – Department of Chemical and Biomolecular Engineering, Johns Hopkins University, Baltimore, Maryland 21218, United States; E-mail: bbukows1@jhu.edu

All authors have given approval to the final version of the manuscript.

ACKNOWLEDGMENTS

MZ and BCB acknowledge the Advanced Research Computing at Hopkins (ARCH) core facility (rockfish.jhu.edu), which is supported by the National Science Foundation (NSF) grant number OAC1920103. MZ and BCB acknowledge support from the Ralph E. Powe Junior Faculty Enhancement Award from Oak Ridge Associated Universities to perform this work.

REFERENCES

(1) Hemelsoet, K.; Van der Mynsbrugge, J.; De Wispelaere, K.; Waroquier, M.; Van Speybroeck, V. Unraveling the Reaction Mechanisms Governing Methanol-to-Olefins Catalysis by Theory and Experiment. *ChemPhysChem* **2013**, *14* (8), 1526–1545. https://doi.org/10.1002/cphc.201201023.

(2) Göltl, F.; Michel, C.; Andrikopoulos, P. C.; Love, A. M.; Hafner, J.; Hermans, I.; Sautet, P. Computationally Exploring Confinement Effects in the Methane-to-Methanol Conversion Over Iron-Oxo Centers in Zeolites. *ACS Catal.* **2016**, *6* (12), 8404–8409. https://doi.org/10.1021/acscatal.6b02640.

(3) Lercher, J. A.; van Santen, R. A.; Vinek, H. Carbonium Ion Formation in Zeolite Catalysis. *Catal Lett* **1994**, *27* (1), 91–96. https://doi.org/10.1007/BF00806981.

(4) Corma, A.; Huber, G. W.; Sauvanaud, L.; O'Connor, P. Processing Biomass-Derived Oxygenates in the Oil Refinery: Catalytic Cracking (FCC) Reaction Pathways and Role of Catalyst. *Journal of Catalysis* **2007**, *247* (2), 307–327. https://doi.org/10.1016/j.jcat.2007.01.023.

(5) Corma, A.; Domine, M. E.; Nemeth, L.; Valencia, S. Al-Free Sn-Beta Zeolite as a Catalyst for the Selective Reduction of Carbonyl Compounds (Meerwein−Ponndorf−Verley Reaction). *J. Am. Chem. Soc.* **2002**, *124* (13), 3194–3195. https://doi.org/10.1021/ja012297m.

(6) Hudson, M. R.; Queen, W. L.; Mason, J. A.; Fickel, D. W.; Lobo, R. F.; Brown, C. M. Unconventional, Highly Selective CO2 Adsorption in Zeolite SSZ-13. *J. Am. Chem. Soc.* **2012**, *134* (4), 1970–1973. https://doi.org/10.1021/ja210580b.

(7) Guo, P.; Shin, J.; Greenaway, A. G.; Min, J. G.; Su, J.; Choi, H. J.; Liu, L.; Cox, P. A.; Hong, S. B.; Wright, P. A.; Zou, X. A Zeolite Family with Expanding Structural Complexity and Embedded Isoreticular Structures. *Nature* **2015**, *524* (7563), 74–78. https://doi.org/10.1038/nature14575.

(8) Kim, C.; Cho, H. S.; Chang, S.; Cho, S. J.; Choi, M. An Ethylenediamine-Grafted y Zeolite: A Highly Regenerable Carbon Dioxide Adsorbent: Via Temperature Swing Adsorption without Urea Formation. *Energy and Environmental Science* **2016**, *9* (5), 1803–1811. https://doi.org/10.1039/c6ee00601a.

(9) Ayodele, O. B. Eliminating Reverse Water Gas Shift Reaction in CO 2 Hydrogenation to Primary Oxygenates over MFI-Type Zeolite Supported Cu/ZnO Nanocatalysts. *Journal of CO2 Utilization* **2017**, *20*, 368–377. https://doi.org/10.1016/j.jcou.2017.06.015.

(10) Kwak, J. H.; Tonkyn, R. G.; Kim, D. H.; Szanyi, J.; Peden, C. H. F. Excellent Activity and Selectivity of Cu-SSZ-13 in the Selective Catalytic Reduction of NOx with NH3. *Journal of Catalysis* **2010**, *275* (2), 187–190. https://doi.org/10.1016/j.jcat.2010.07.031.

(11) Xu, Y.; Zheng, M.; Musgrave, C. B. I.; Zhang, L.; Goddard, W. A. I.; Bukowski, B. C.; Liu, Y. Assessing the Kinetics of Quinone–CO2 Adduct Formation for Electrochemically Mediated Carbon Capture. *ACS Sustainable Chem. Eng.* **2023**, *11* (30), 11333–11341. https://doi.org/10.1021/acssuschemeng.3c03321.

(12) Zhang, J.; Wegener, E. C.; Samad, N. R.; Harris, J. W.; Unocic, K. A.; Allard, L. F.; Purdy, S.; Adhikari, S.; Cordon, M. J.; Miller, J. T.; Krause, T. R.; Cheng, S.; Liu, D.; Li, M.; Jiang, X.; Wu, Z.; Li, Z. Isolated Metal Sites in Cu–Zn–Y/Beta for Direct and Selective Butene-Rich C_{3+} Olefin Formation from Ethanol. *ACS Catal.* **2021**, *11* (15), 9885–9897. https://doi.org/10.1021/acscatal.1c02177.

(13) Muñoz-Guerra, S.; Lavilla, C.; Japu, C.; Ilarduya, A. M. de. Renewable Terephthalate Polyesters from Carbohydrate-Based Bicyclic Monomers. *Green Chem.* **2014**, *16* (4), 1716–1739. https://doi.org/10.1039/C3GC42394H.

(14) Silva, C. X. A. da; Gonçalves, V. L. C.; Mota, C. J. A. Water-Tolerant Zeolite Catalyst for the Acetalisation of Glycerol. *Green Chem.* **2009**, *11* (1), 38–41. https://doi.org/10.1039/B813564A.

(15) Jin, M.; Ravi, M.; Lei, C.; Heard, C. J.; Brivio, F.; Tošner, Z.; Grajciar, L.; van Bokhoven, J. A.; Nachtigall, P. Dynamical Equilibrium between Brønsted and Lewis Sites in Zeolites: Framework-Associated Octahedral Aluminum. *Angewandte Chemie International Edition n/a* (n/a), e202306183. https://doi.org/10.1002/anie.202306183.

(16) Tang, X.; Chen, W.; Dong, W.; Liu, Z.; Yuan, J.; Xia, H.; Yi, X.; Zheng, A. Framework Aluminum Distribution in ZSM-5 Zeolite Directed by Organic Structure-Directing Agents: A Theoretical Investigation. *Catalysis Today* **2022**, *405–406*, 101–110. https://doi.org/10.1016/j.cattod.2022.06.027.

(17) Csicsery, S. M. Shape-Selective Catalysis in Zeolites. *Zeolites* **1984**, *4* (3), 202–213. https://doi.org/10.1016/0144-2449(84)90024-1.

(18) Liu, X.; Liu, S.; Yan, T.; Shang, N.; Li, H.; Wang, Z.; Xu, H.; Wu, P. Tin Active Sites Confined in Zeolite Framework as a Promising Shape-Selective Catalyst for Ethylene Oxide Hydration. *Chemistry – A European Journal* **2023**, *29* (16), e202203696. https://doi.org/10.1002/chem.202203696.

(19) Svelle, S.; Olsbye, U.; Joensen, F.; Bjørgen, M. Conversion of Methanol to Alkenes over Medium- and Large-Pore Acidic Zeolites: Steric Manipulation of the Reaction Intermediates Governs the Ethene/Propene Product Selectivity. *J. Phys. Chem. C* **2007**, *111* (49), 17981–17984. https://doi.org/10.1021/jp077331j.

(20) Brogaard, R. Y.; Wang, C.-M.; Studt, F. Methanol–Alkene Reactions in Zeotype Acid Catalysts: Insights from a Descriptor-Based Approach and Microkinetic Modeling. *ACS Catal.* **2014**, *4* (12), 4504–4509. https://doi.org/10.1021/cs5014267.

(21) Iglesia, E. Design, Synthesis, and Use of Cobalt-Based Fischer-Tropsch Synthesis Catalysts. *Applied Catalysis A: General* **1997**, *161* (1), 59–78. https://doi.org/10.1016/S0926-860X(97)00186-5.

(22) Jacobs, G.; Ma, W.; Davis, B. H. Influence of Reduction Promoters on Stability of Cobalt/g-Alumina Fischer-Tropsch Synthesis Catalysts. *Catalysts* **2014**, *4* (1), 49–76. https://doi.org/10.3390/catal4010049.

(23) Li, G.; Wang, B.; Resasco, D. E. Water-Mediated Heterogeneously Catalyzed Reactions. *ACS Catal.* **2020**, *10* (2), 1294–1309. https://doi.org/10.1021/acscatal.9b04637.

(24) Chen, K.; Kelsey, J.; White, J. L.; Zhang, L.; Resasco, D. Water Interactions in Zeolite Catalysts and Their Hydrophobically Modified Analogues. *ACS Catal.* **2015**, *5* (12), 7480–7487. https://doi.org/10.1021/acscatal.5b02040.

(25) Zapata, P. A.; Faria, J.; Ruiz, M. P.; Jentoft, R. E.; Resasco, D. E. Hydrophobic Zeolites for Biofuel Upgrading Reactions at the Liquid–Liquid Interface in Water/Oil Emulsions. *J. Am. Chem. Soc.* **2012**, *134* (20), 8570–8578. https://doi.org/10.1021/ja3015082.

(26) Bregante, D. T.; Johnson, A. M.; Patel, A. Y.; Ayla, E. Z.; Cordon, M. J.; Bukowski, B. C.; Greeley, J.; Gounder, R.; Flaherty, D. W. Cooperative Effects between Hydrophilic Pores and Solvents: Catalytic Consequences of Hydrogen Bonding on Alkene Epoxidation in Zeolites. *J. Am. Chem. Soc.* **2019**, *141* (18), 7302–7319. https://doi.org/10.1021/jacs.8b12861.

(27) Yu, Q.; Bowman, J. M. High-Level Quantum Calculations of the IR Spectra of the Eigen, Zundel, and Ring Isomers of $H^+(H_2O)_4$ Find a Single Match to Experiment. *J. Am. Chem. Soc.* **2017**, *139* (32), 10984–10987. https://doi.org/10.1021/jacs.7b05459.

(28) Mei, D.; Lercher, J. A. Effects of Local Water Concentrations on Cyclohexanol Dehydration in H-BEA Zeolites. *J. Phys. Chem. C* **2019**, *123* (41), 25255–25266. https://doi.org/10.1021/acs.jpcc.9b07738.

(29) Cordon, M. J.; Harris, J. W.; Vega-Vila, J. C.; Bates, J. S.; Kaur, S.; Gupta, M.; Witzke, M. E.; Wegener, E. C.; Miller, J. T.; Flaherty, D. W.; Hibbitts, D. D.; Gounder, R. Dominant Role of Entropy in Stabilizing Sugar Isomerization Transition States within Hydrophobic

Zeolite Pores. *J. Am. Chem. Soc.* **2018**, *140* (43), 14244–14266. https://doi.org/10.1021/jacs.8b08336.
(30) Grifoni, E.; Piccini, G.; Lercher, J. A.; Glezakou, V.-A.; Rousseau, R.; Parrinello, M. Confinement Effects and Acid Strength in Zeolites. *Nat Commun* **2021**, *12* (1), 2630. https://doi.org/10.1038/s41467-021-22936-0.
(31) Bates, J. S.; Bukowski, B. C.; Greeley, J.; Gounder, R. Structure and Solvation of Confined Water and Water–Ethanol Clusters within Microporous Brønsted Acids and Their Effects on Ethanol Dehydration Catalysis. *Chem. Sci.* **2020**, *11* (27), 7102–7122. https://doi.org/10.1039/D0SC02589E.
(32) Berens, P. H.; Mackay, D. H. J.; White, G. M.; Wilson, K. R. Thermodynamics and Quantum Corrections from Molecular Dynamics for Liquid Water. *The Journal of Chemical Physics* **1983**, *79* (5), 2375–2389. https://doi.org/10.1063/1.446044.
(33) Jorgensen, W. L.; Chandrasekhar, J.; Madura, J. D.; Impey, R. W.; Klein, M. L. Comparison of Simple Potential Functions for Simulating Liquid Water. *The Journal of Chemical Physics* **1983**, *79* (2), 926–935. https://doi.org/10.1063/1.445869.
(34) Seki, T.; Chiang, K.-Y.; Yu, C.-C.; Yu, X.; Okuno, M.; Hunger, J.; Nagata, Y.; Bonn, M. The Bending Mode of Water: A Powerful Probe for Hydrogen Bond Structure of Aqueous Systems. *J. Phys. Chem. Lett.* **2020**, *11* (19), 8459–8469. https://doi.org/10.1021/acs.jpclett.0c01259.
(35) van Duin, A. C. T.; Dasgupta, S.; Lorant, F.; Goddard, W. A. ReaxFF: A Reactive Force Field for Hydrocarbons. *J. Phys. Chem. A* **2001**, *105* (41), 9396–9409. https://doi.org/10.1021/jp004368u.
(36) van Duin, A. C. T.; Strachan, A.; Stewman, S.; Zhang, Q.; Xu, X.; Goddard, W. A. ReaxFFSiO Reactive Force Field for Silicon and Silicon Oxide Systems. *J. Phys. Chem. A* **2003**, *107* (19), 3803–3811. https://doi.org/10.1021/jp0276303.
(37) Naserifar, S.; Chen, Y.; Kwon, S.; Xiao, H.; Goddard, W. A. Artificial Intelligence and QM/MM with a Polarizable Reactive Force Field for Next-Generation Electrocatalysts. *Matter* **2021**, *4* (1), 195–216. https://doi.org/10.1016/j.matt.2020.11.010.
(38) Jinnouchi, R.; Karsai, F.; Kresse, G. On-the-Fly Machine Learning Force Field Generation: Application to Melting Points. *Phys. Rev. B* **2019**, *100* (1), 014105. https://doi.org/10.1103/PhysRevB.100.014105.
(39) Liu, P.; Verdi, C.; Karsai, F.; Kresse, G. $\ensuremath{\alpha}\text{\ensuremath{-}}\ensuremath{\beta}$ Phase Transition of Zirconium Predicted by on-the-Fly Machine-Learned Force Field. *Phys. Rev. Mater.* **2021**, *5* (5), 053804. https://doi.org/10.1103/PhysRevMaterials.5.053804.
(40) Verdi, C.; Karsai, F.; Liu, P.; Jinnouchi, R.; Kresse, G. Thermal Transport and Phase Transitions of Zirconia by On-the-Fly Machine-Learned Interatomic Potentials. *npj Comput Mater* **2021**, *7* (1), 1–9. https://doi.org/10.1038/s41524-021-00630-5.
(41) Zhang, G.; Liu, W.; Hu, T.; Shuai, S.; Chen, C.; Xu, S.; Ren, W.; Wang, J.; Ren, Z. On-the-Fly Machine Learning Force Field Study of Liquid-Al/α-Al2O3 Interface. *Applied Surface Science* **2023**, 158141. https://doi.org/10.1016/j.apsusc.2023.158141.
(42) Liu, P.; Wang, J.; Avargues, N.; Verdi, C.; Singraber, A.; Karsai, F.; Chen, X.-Q.; Kresse, G. Combining Machine Learning and Many-Body Calculations: Coverage-Dependent Adsorption of CO on Rh(111). *Phys. Rev. Lett.* **2023**, *130* (7), 078001. https://doi.org/10.1103/PhysRevLett.130.078001.
(43) Xia, D.; Chen, J.; Xie, H.-B.; Zhong, J.; Francisco, J. S. Counterintuitive Oxidation of Alcohols at Air–Water Interfaces. *J. Am. Chem. Soc.* **2023**, *145* (8), 4791–4799. https://doi.org/10.1021/jacs.2c13661.
(44) Roy, S.; Dürholt, J. P.; Asche, T. S.; Zipoli, F.; Gómez-Bombarelli, R. Learning a Reactive Potential for Silica-Water through Uncertainty Attribution. arXiv July 4, 2023. https://doi.org/10.48550/arXiv.2307.01705.
(45) Erlebach, A.; Šípka, M.; Saha, I.; Nachtigall, P.; Heard, C. J.; Grajciar, L. A Reactive Neural Network Framework for Water-Loaded Acidic Zeolites. arXiv July 13, 2023. https://doi.org/10.48550/arXiv.2307.00911.
(46) Saha, I.; Erlebach, A.; Nachtigall, P.; Heard, C. J.; Grajciar, L. Quantifying the Effect of Si/Al Ratio on Proton Solvation and Water Diffusion in H-FAU Using Reactive Neural Network Potential. ChemRxiv July 12, 2023. https://doi.org/10.26434/chemrxiv-2022-d1sj9-v3.
(47) *Database of Zeolite Structures*. http://www.iza-structure.org/databases/ (accessed 2023-04-30).
(48) Hjorth Larsen, A.; Jørgen Mortensen, J.; Blomqvist, J.; Castelli, I. E.; Christensen, R.; Dułak, M.; Friis, J.; Groves, M. N.; Hammer, B.; Hargus, C.; Hermes, E. D.; Jennings, P. C.; Bjerre Jensen, P.; Kermode, J.; Kitchin, J. R.; Leonhard Kolsbjerg, E.; Kubal, J.; Kaasbjerg, K.; Lysgaard, S.; Bergmann Maronsson, J.; Maxson, T.; Olsen, T.; Pastewka, L.; Peterson, A.; Rostgaard, C.; Schiøtz, J.; Schütt, O.; Strange, M.; Thygesen, K. S.; Vegge, T.; Vilhelmsen, L.; Walter, M.; Zeng, Z.; Jacobsen, K. W. The Atomic Simulation Environment—a Python Library for Working with Atoms. *J. Phys.: Condens. Matter* **2017**, *29* (27), 273002. https://doi.org/10.1088/1361-648X/aa680e.
(49) Kresse, G.; Hafner, J. Ab Initio Molecular-Dynamics Simulation of the Liquid-Metal--Amorphous-Semiconductor Transition in Germanium. *Phys. Rev. B* **1994**, *49* (20), 14251–14269. https://doi.org/10.1103/PhysRevB.49.14251.
(50) Kresse, G.; Hafner, J. *Ab Initio* Molecular Dynamics for Liquid Metals. *Phys. Rev. B* **1993**, *47* (1), 558–561. https://doi.org/10.1103/PhysRevB.47.558.
(51) Kresse, G.; Furthmüller, J. Efficient Iterative Schemes for *Ab Initio* Total-Energy Calculations Using a Plane-Wave Basis Set. *Phys. Rev. B* **1996**, *54* (16), 11169–11186. https://doi.org/10.1103/PhysRevB.54.11169.
(52) Kresse, G.; Furthmüller, J. Efficiency of Ab-Initio Total Energy Calculations for Metals and Semiconductors Using a Plane-Wave Basis Set. *Computational Materials Science* **1996**, *6* (1), 15–50. https://doi.org/10.1016/0927-0256(96)00008-0.
(53) Perdew, J. P.; Burke, K.; Ernzerhof, M. Generalized Gradient Approximation Made Simple. *Phys. Rev. Lett.* **1996**, *77* (18), 3865–3868. https://doi.org/10.1103/PhysRevLett.77.3865.
(54) Grimme, S.; Ehrlich, S.; Goerigk, L. Effect of the Damping Function in Dispersion Corrected Density

Functional Theory. *J. Comput. Chem.* **2011**, *32* (7), 1456–1465. https://doi.org/10.1002/jcc.21759.
(55) Stanciakova, K.; Louwen, J. N.; Weckhuysen, B. M.; Bulo, R. E.; Göltl, F. Understanding Water–Zeolite Interactions: On the Accuracy of Density Functionals. *J. Phys. Chem. C* **2021**, *125* (37), 20261–20274. https://doi.org/10.1021/acs.jpcc.1c04270.
(56) Evans, D. J.; Holian, B. L. The Nose–Hoover Thermostat. *The Journal of Chemical Physics* **1985**, *83* (8), 4069–4074. https://doi.org/10.1063/1.449071.
(57) Jinnouchi, R.; Karsai, F.; Verdi, C.; Asahi, R.; Kresse, G. Descriptors Representing Two- and Three-Body Atomic Distributions and Their Effects on the Accuracy of Machine-Learned Inter-Atomic Potentials. *J. Chem. Phys.* **2020**, *152* (23), 234102. https://doi.org/10.1063/5.0009491.
(58) Jinnouchi, R.; Lahnsteiner, J.; Karsai, F.; Kresse, G.; Bokdam, M. Phase Transitions of Hybrid Perovskites Simulated by Machine-Learning Force Fields Trained on the Fly with Bayesian Inference. *Phys. Rev. Lett.* **2019**, *122* (22), 225701. https://doi.org/10.1103/PhysRevLett.122.225701.
(59) Bartók, A. P.; Csányi, G. Gaussian Approximation Potentials: A Brief Tutorial Introduction. arXiv February 5, 2020. http://arxiv.org/abs/1502.01366 (accessed 2023-04-29).
(60) Bartók, A. P.; Kondor, R.; Csányi, G. On Representing Chemical Environments. *Phys. Rev. B* **2013**, *87* (18), 184115. https://doi.org/10.1103/PhysRevB.87.184115.
(61) Miwa, K.; Ohno, H. Molecular Dynamics Study on β - Phase Vanadium Monohydride with Machine Learning Potential. *Phys. Rev. B* **2016**, *94* (18), 184109. https://doi.org/10.1103/PhysRevB.94.184109.
(62) Bukowski, B. C.; Bates, J. S.; Gounder, R.; Greeley, J. Defect-Mediated Ordering of Condensed Water Structures in Microporous Zeolites. *Angew. Chem. Int. Ed.* **2019**, *58* (46), 16422–16426. https://doi.org/10.1002/anie.201908151.
(63) Loewenstein, W. The Distribution of Aluminum in the Tetrahedra of Silicates and Aluminates. *American Mineralogist* **1954**, *39* (1–2), 92–96.
(64) Hack, J. H.; Ma, X.; Chen, Y.; Dombrowski, J. P.; Lewis, N. H. C.; Li, C.; Kung, H. H.; Voth, G. A.; Tokmakoff, A. Proton Dissociation and Delocalization under Stepwise Hydration of Zeolite HZSM-5. *J. Phys. Chem. C* **2023**, *127* (32), 16175–16186. https://doi.org/10.1021/acs.jpcc.3c03611.
(65) Cukierman, S. Et Tu, Grotthuss! And Other Unfinished Stories. *Biochimica et Biophysica Acta (BBA) - Bioenergetics* **2006**, *1757* (8), 876–885. https://doi.org/10.1016/j.bbabio.2005.12.001.
(66) Mei, D.; Lercher, J. A. Mechanistic Insights into Aqueous Phase Propanol Dehydration in H-ZSM-5 Zeolite. *AIChE Journal* **2017**, *63* (1), 172–184. https://doi.org/10.1002/aic.15517.
(67) Wang, M.; Jaegers, N. R.; Lee, M.-S.; Wan, C.; Hu, J. Z.; Shi, H.; Mei, D.; Burton, S. D.; Camaioni, D. M.; Gutiérrez, O. Y.; Glezakou, V.-A.; Rousseau, R.; Wang, Y.; Lercher, J. A. Genesis and Stability of Hydronium Ions in Zeolite Channels. *J. Am. Chem. Soc.* **2019**, *141* (8), 3444–3455. https://doi.org/10.1021/jacs.8b07969.
(68) Dalla Bernardina, S.; Paineau, E.; Brubach, J.-B.; Judeinstein, P.; Rouzière, S.; Launois, P.; Roy, P. Water in Carbon Nanotubes: The Peculiar Hydrogen Bond Network Revealed by Infrared Spectroscopy. *J. Am. Chem. Soc.* **2016**, *138* (33), 10437–10443. https://doi.org/10.1021/jacs.6b02635.